

## Article

# A Novel Strategy for the Synthesis of High Stability of Luminescent Zero Dimensional–Two Dimensional CsPbBr<sub>3</sub> Quantum Dot/1,4-bis(4-methylstyryl)benzene Nanoplate Heterostructures at an Atmospheric Condition

Yanran Wang<sup>1,2</sup>, Ming-yu Li<sup>1,2,\*</sup>, Shijie Liu<sup>2</sup>, Yuan Ma<sup>2</sup>, Bo Sun<sup>2</sup>, Liangyu Wang<sup>2</sup>, Haifei Lu<sup>2</sup>, Xiaoyan Wen<sup>2</sup>, Sisi Liu<sup>2,\*</sup> and Xumin Ding<sup>3</sup>

<sup>1</sup> Donghai Laboratory, Zhoushan 316021, China; 312506@whut.edu.cn

<sup>2</sup> School of Science, Wuhan University of Technology, Wuhan 430070, China; liusj@whut.edu.cn (S.L.); 327402@whut.edu.cn (Y.M.); 285422@whut.edu.cn (B.S.); 333616@whut.edu.cn (L.W.); haifeilv@whut.edu.cn (H.L.); wenxy@whut.edu.cn (X.W.)

<sup>3</sup> Advanced Microscopy and Instrumentation Research Center, School of Instrumentation Science and Engineering, Harbin Institute of Technology, Harbin 150090, China; xuminding@hit.edu.cn

\* Correspondence: mingyu.li.oliver@gmail.com (M.-y.L.); liusisi0109@hotmail.com (S.L.)

**Abstract:** Perovskite quantum dots (QDs), emerging with excellent bright-green photoluminescence (PL) and a large absorption coefficient, are of great potential for the fabrication of light sources in underwater optical wireless communication systems. However, the instability caused by low formation energy and abundant surface traps is still a major concern for perovskite-based light sources in underwater conditions. Herein, we propose ultra-stable zero dimensional–two dimensional (0D–2D) CsPbBr<sub>3</sub> QD/1,4-bis(4-methylstyryl)benzene (*p*-MSB) nanoplate (NP) heterostructures synthesized via a facile approach at room temperature in air. CsPbBr<sub>3</sub> QDs can naturally nucleate on the *p*-MSB NP toluene solution, and the radiative combination is drastically intensified owing to the electron transfer within the typical type-II heterostructures, leading to a sharply increased PLQY of the heterostructure thin films up to 200% compared with the pristine sample. The passivation of defects within CsPbBr<sub>3</sub> QDs can be effectively realized with the existence of *p*-MSB NPs, and thus the obviously improved PL is steadily witnessed in an ambient atmosphere and thermal environment. Meanwhile, the enhanced humidity stability and a peak EQE of 9.67% suggests a synergetic strategy for concurrently addressing the knotty problems on unsatisfied luminous efficiency and stability of perovskites for high-performance green-emitting optoelectronic devices in underwater applications.

**Keywords:** perovskite quantum dots; *p*-MSB nanoplate; typical type-II heterostructure; high photoluminescence quantum yield; moisture stability



**Citation:** Wang, Y.; Li, M.-y.; Liu, S.; Ma, Y.; Sun, B.; Wang, L.; Lu, H.; Wen, X.; Liu, S.; Ding, X. A Novel Strategy for the Synthesis of High Stability of Luminescent Zero Dimensional–Two Dimensional CsPbBr<sub>3</sub> Quantum Dot/1,4-bis(4-methylstyryl)benzene Nanoplate Heterostructures at an Atmospheric Condition.

*Nanomaterials* **2023**, *13*, 2723.

<https://doi.org/10.3390/nano13192723>

Academic Editor: Alain Pignolet

Received: 22 August 2023

Revised: 27 September 2023

Accepted: 29 September 2023

Published: 7 October 2023



**Copyright:** © 2023 by the authors. Licensee MDPI, Basel, Switzerland. This article is an open access article distributed under the terms and conditions of the Creative Commons Attribution (CC BY) license (<https://creativecommons.org/licenses/by/4.0/>).

## 1. Introduction

In recent years, the fabrication of high-performance light-emitting diodes (LEDs) and laser diodes (LDs) has drawn ever-growing research interests as light sources for underwater optical wireless communication (UOWC) systems [1] owing to their diverse potential applications in submarine communications, deep ocean exploration and underwater wireless sensor networks (UWSNs), etc. [2–4]. Recently, metal halide perovskites (MHPs) have been regarded as promising solid-state light-emission materials in LEDs and gain mediums in LDs because of their excellent photoluminescence quantum yield (PLQY), superior exciton binding energy, narrow emission, and tunable bandgap [5,6]. Among MHPs, cesium lead halide quantum dots (CsPbBr<sub>3</sub> QDs) exhibit excellent scintillation properties [7,8], outstanding bright-green photoluminescence (PL), and high PLQY [9], which have been witnessed near-unity PLQYs in solution [10]. However, the agglomeration of nanocrystals during the fabrication of thin films can potentially result in the severe deterioration of PLQY,

down to 18% [11], in association with loss of quantum confinement [12], and thus a feasible strategy on the realization of highly luminescent thin films with perovskite QDs is still a crucial problem for application in light-emitting devices [13]. Providing the low formation energy [14] and mobile ionic structure with abundant surface traps [15], perovskites are generally vulnerable to external factors, including oxygen, temperature, and moisture [16], inherently hindering the development of high-performance underwater light sources [17].

To date, numerous researches have increasingly endeavored to explore an effective approach for improving the stability of CsPbBr<sub>3</sub> QDs [14], and a popular routine strategy is to construct relatively inert shells or barrier matrixes among the QDs, preventing the undesirable erosion of oxygen and moisture [18]. For instance, the uniform CsPbBr<sub>3</sub>@CdS core/shell QDs were synthesized with significantly improved stability under 75% relative humidity (RH) at the expense of the slightly decreased PLQY for the colloidal QD solution from 90% to 88% [19]. Meanwhile, the mono-dispersed CsPbBr<sub>3</sub>@SiO<sub>2</sub> colloidal QDs were synthesized at −20 °C with the enhanced PLQY for the solution of blue emission at 460 nm from 72.4% to 75.6% [20]. Unfortunately, the surface passivation with inorganic oxides was inevitably porous due to the lattice mismatch between CsPbBr<sub>3</sub> and SiO<sub>2</sub> [21], which can suffer a high permeable possibility of external H<sub>2</sub>O/O<sub>2</sub> [22]. To minimize the lattice mismatch between foreign materials, CsPbBr<sub>x</sub> shells were grown in situ on CsPbBr<sub>3</sub> QDs via a facile hot injection method, and the blue emission PLQY of CsPbBr<sub>3</sub>@Amorphous-CsPbBr<sub>x</sub> QD solution was radically increased from 54% to 84% in comparison with pristine cubic CsPbBr<sub>3</sub> QD solution under excitation of 365 nm light illumination [23]. Despite a noticeably improved PLQY, the decomposition of the CsPbBr<sub>x</sub> still remains a big concern under exposure to moisture and oxygen [22,24]. Additionally, perovskite quantum dots can also be packed into crosslinked polystyrene (PS) beads via a simple swelling–shrinking strategy, which exhibited an extraordinary water-resistant property [25]. Meanwhile, the construction of non-luminescent polymer matrixes can somewhat sacrifice effective area, in turn leading to undesirable irradiation attenuation [26]. Therefore, a well-balanced approach between long-term stability and high PLQY is currently a critical obstacle for the CsPbBr<sub>3</sub> QDs as light-emission materials of light sources in particle applications [13,27].

Here, we demonstrate a synthetic strategy to simultaneously enhance the PLQY and stability under various conditions with a novel zero dimensional–two dimensional (0D–2D) CsPbBr<sub>3</sub> quantum dot (QD)/1,4-bis(4-methylstyryl)benzene (*p*-MSB) nanoplate (NP) heterostructures. The 0D–2D heterostructures were facilely synthesized via spontaneous nucleation of CsPbBr<sub>3</sub> QDs on *p*-MSB nanoplates at room temperature under an atmosphere condition, and the PLQY of the resulting thin films radically increased by 200% with an optimized blending concentration of *p*-MSB at 1mg/mL owing to the photoactive carrier transfer from *p*-MSB NPs to CsPbBr<sub>3</sub> QDs. Benefiting from the hydrophobicity of *p*-MSB, the heterostructure thin films constantly exhibits an outstanding stability under various temperatures throughout the whole testing duration, which is theoretically discussed with the density functional theory (DFT) calculations. Eventually, the 0D–2D CsPbBr<sub>3</sub> QD/*p*-MSB heterostructures are engaged for the fabrication of green-emitting LEDs with an external quantum efficiency (EQE) of up to 9.67%.

## 2. Materials and Methods

Chemicals: Cesium carbonate (Cs<sub>2</sub>CO<sub>3</sub>, 99%, Aladdin, Riverside, CA, USA), propionic acid (C<sub>3</sub>H<sub>6</sub>O<sub>2</sub> ≥ 99.5%, SCRC), lead(II) bromide (PbBr<sub>2</sub>, 99.99%, Aladdin), butylamine (C<sub>4</sub>H<sub>11</sub>N, 99.5%, Aladdin), isopropanol (C<sub>3</sub>H<sub>8</sub>O ≥ 99.7%, SCRC), 1,4-Bis(4-methylstyryl)benzene (C<sub>24</sub>H<sub>22</sub> > 98%, TCI) (*p*-MSB), n-hexane (C<sub>6</sub>H<sub>14</sub> ≥ 97%, SCRC), and toluene (C<sub>7</sub>H<sub>8</sub> ≥ 99.5%, SCRC).

Preparation of hybrid CsPbBr<sub>3</sub> QD/*p*-MSB nanoplates solutions: The Cs<sup>+</sup> precursor was initially prepared by dissolving 0.5868 g Cs<sub>2</sub>CO<sub>3</sub> powders into 1 mL propionic acid under ultra-sonification at room temperature, and 25 μL Cs<sup>+</sup> precursor was subsequently injected into a mixture of 5 mL isopropanol and 10 mL n-hexane, followed by vigorous stirring for 2 min. Meanwhile, 0.9175 g PbBr<sub>2</sub> powders were dissolved in a 5 mL mixed

solution of butylamine, isopropanol, and propionic acid with a volume ratio of 1:1:1. Finally, CsPbBr<sub>3</sub> QDs were synthesized by swiftly adding 0.27 mL PbBr<sub>2</sub> solution into the as-prepared Cs<sup>+</sup> precursor under ambient conditions and were dispersed in the 8 mL toluene solution with various *p*-MSB concentrations between 0 and 2 mg/mL after a centrifugation process at 2000 r/min for two minutes, respectively.

Deposition of the hybrid thin films: Prior to the deposition, each glass substrate with a size of 2.5 × 2.5 cm<sup>2</sup> was cleaned via a series of sonicate treatments in deionized (DI) water, ethanol, and acetone for 20 min. After drying with nitrogen, the CsPbBr<sub>3</sub> QD/*p*-MSB nanoplate hybrid thin films were deposited by a sequential spin-coating process on glass substrates at 500 rpm for 20 s and 2000 rpm for 40 s, and the thin films were immediately treated with an annealing procedure at 80 °C for 1 min to evaporate the solvent and remove organic residuals. The devices were fabricated after 3 depositions, and then were annealed at 80 °C for 5 min to guarantee crystallization.

Device characterization: The transmission electron microscope (TEM, FEI Tecnai G2 F20, FEI Co., Hillsboro, OR, USA) was employed for topological characterization of hybrid nanostructures. The surface morphologies of the resulting samples were characterized with a scanning electron microscope (SEM, Hitachi, Tokyo, Japan), and the corresponding elementary analysis was performed with an integrated energy-dispersive spectroscopy system (EDS, Regulus 8100, Hitachi, Tokyo, Japan). The room temperature photoluminescence (PL) and UV-Vis absorption spectra were recorded with a Shimadzu RF-6000 Spectro fluorophotometer (Kyoto, Japan) and a Shimadzu UV-2600 spectrophotometer (Kyoto, Japan) with an excitation light of 350 nm, respectively. Fluorescence quantum yields (PLQY) (relative values) of samples were calculated according to the following expression:

$$Y_u = Y_s \times \frac{F_u}{F_s} \times \frac{A_s}{A_u} \quad (1)$$

where  $Y_s$  is the fluorescence quantum yield to the reference,  $F_s$  and  $F_u$  are the integral fluorescence intensity of the reference and sample, and  $A_s$  and  $A_u$  are the absorbance at the excitation wavelength of the sample and reference, respectively. The reference materials selected for the PLQY calculation of solutions and films were rhodamine B (quantum yield 89%) and standard sample (quantum yield 55%). The surface roughness conformed with an atomic force microscopy (AFM, Dimension Icon, Bruker, Karlsruhe, Germany), and X-ray diffraction (XRD) measurements were carried out by a Japan Rigaku Smartlab SE diffractometer with a Cu K $\alpha$  radiation source. Raman spectra were obtained at room temperature using a LabRAM HR Evolution Horiba spectrometer. The time-resolved PL (TRPL) spectra were obtained with a spectrophotometer (Edinburgh FLS1000, Edinburgh Company, Edinburgh, UK), and an X-ray photoelectron instrument (ESCALAB Xi+, Thermo Fisher Scientific, Waltham, MA, USA) was used for the X-ray photoelectron spectroscopy (XPS) images for each sample. Supersaturated salt solutions of LiF, NaCl, and KCl (25 °C) in a sealed chamber were employed to achieve a relative humidity (RH) level of 30%, 75%, and 84%, respectively.

Water molecule adsorption simulation: The absorption energy for water molecules on the surface of the hybrid CsPbBr<sub>3</sub> QD/*p*-MSB nanoplates was calculated based on the density functional theory (DFT). The exchange–correlation between electrons was described by the generalized gradient approximation (GGA) in the Perdew–Burke–Ernzerhof (PBE) form. A cut-off energy of 300 eV was chosen for the plane-wave basis set in all calculations. The relaxation of geometry optimization was continued until the residual force was less than 0.05 eV/Å and the total energy was lower than  $2 \times 10^{-5}$  eV per atom. The Monkhorst–Pack k-point mesh of  $5 \times 5 \times 2$  was used for the geometry optimizations and static electronic structure calculations. A vacuum slab of 20 Å was introduced to provide enough distance for the hindrance of interactions between layers.

### 3. Results and Discussion

Figure 1a illustrates the fabrication process of zero dimensional–two dimensional (0D–2D) CsPbBr<sub>3</sub> quantum dot (QD)/*p*-MSB nanoplate (NP) thin films, and the corresponding morphologies of the CsPbBr<sub>3</sub> QD/*p*-MSB NP heterostructures are shown in Figure 1b–d. To be specific, CsPbBr<sub>3</sub> QDs were simply obtained by a liquid-phase reaction between PbBr<sub>2</sub> and Cs<sup>+</sup> precursor solutions at room temperature under atmospheric conditions, and the as-synthesized CsPbBr<sub>3</sub> QDs were blended with *p*-MSB NPs with a variation of concentrations between 0 and 2 mg/mL, as depicted in Figure 1a. As shown in Figure 1b, the CsPbBr<sub>3</sub> QDs uniformly decorated on the surface of *p*-MSB NPs. As evidenced with clear lattice fringes shown in Figure 1c,d, the resulting CsPbBr<sub>3</sub> QDs on *p*-MSB NPs exhibited excellent crystallinity [28], and the interplanar distance of 4.2 Å can be assigned to the (110) crystal plane of the cubic perovskite [29]. Figure S1 shows the typical diffraction rings corresponding to the (001), (011), and (012) planes [30,31] within the perovskite structure, suggesting a well-defined crystalline structure of CsPbBr<sub>3</sub> QDs on *p*-MSB NPs [32].

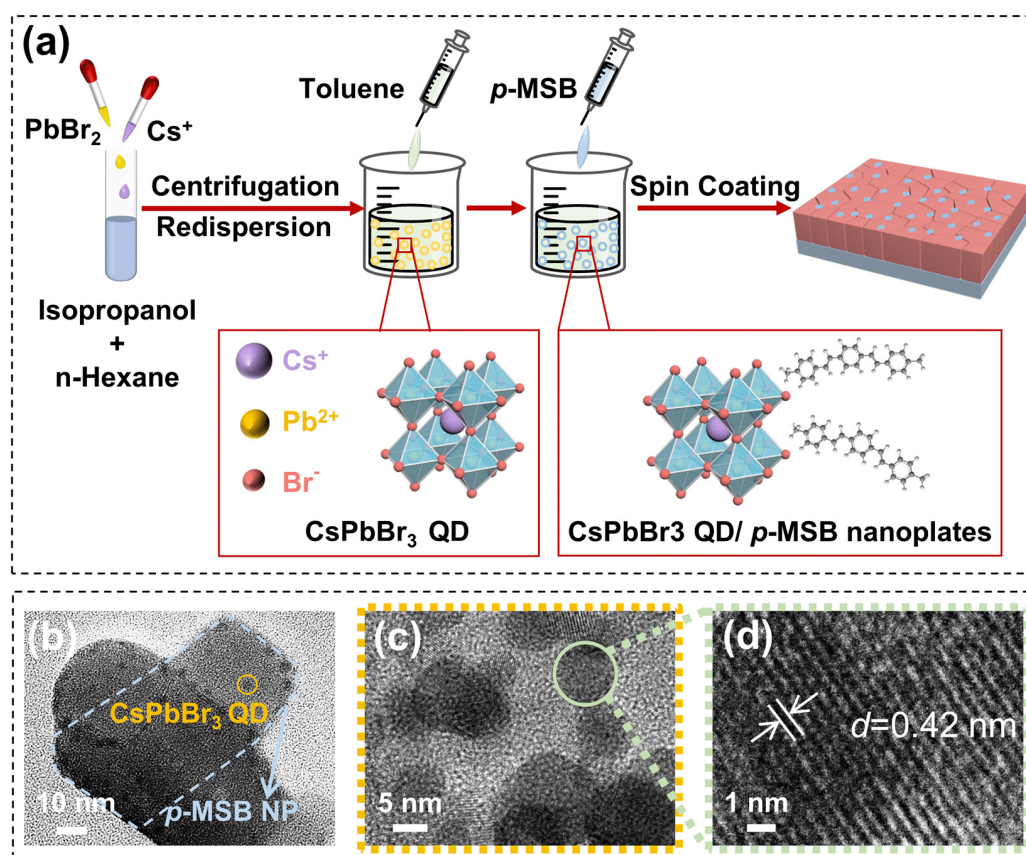


**Figure 1.** (a) Schematic illustration for the fabrication process of 0D–2D CsPbBr<sub>3</sub> QD/*p*-MSB NP thin films. The transmission electron microscope (TEM) images of (b) CsPbBr<sub>3</sub> QDs on *p*-MSB NP and (c,d) CsPbBr<sub>3</sub> QDs at different magnifications.

To investigate the evolution of optical properties, a series of characterizations was applied for the 0D–2D CsPbBr<sub>3</sub> QD/*p*-MSB NP solutions depending on the *p*-MSB concentrations: 2 mg/mL (Sp1), 1 mg/mL (Sp2), 0.5 mg/mL (Sp3), 0.1 mg/mL (Sp4), 0.05 mg/mL (Sp5), 0.025 mg/mL (Sp6), 0 mg/mL (Sp7). As shown in Figure 2a, each sample exhibited an identical absorption edge at ~530 nm in the spectra, confirming a negligible effect of the *p*-MSB concentrations on the crystal structure and size distribution of CsPbBr<sub>3</sub> QDs [33]. With the elevated *p*-MSB concentrations, the absorption curves slightly bent down above 400 nm, which can be inherited from the behavior of the *p*-MSB NPs as evidenced by the

absorbance spectrum in Figure S2a. As depicted with the Tauc plots in Figure S2b, the 0D–2D heterostructures correspondingly maintained a comparable optical bandgap of  $\sim 2.35$  eV regardless of the *p*-MSB concentrations. Furthermore, as shown in Figure S2c, the absorption coefficient near the band edge was modeled by using Elliot's theory of Wannier excitons [34] to assign the contributions from the excitonic peak (blue dashed line) and the lowest band of the continuum transition (green dashed line), respectively [35]. As such, we are able to extract the continuum absorption onset energy, that is, the bandgap energy  $E_g \approx 2.200$  eV, as well as the center of exciton resonance  $E_0 \approx 2.192$  eV. The exciton binding energy  $R_{ex} \approx 7.911$  meV is then determined by their difference:  $R_{ex} = E_g - E_0$ . The room temperature photoluminescence (PL) spectra for each sample were recorded with 350 nm light excitation as shown in Figure 2b, and the elevated intensity of excitonic emission at 526 nm was constantly witnessed with the increased *p*-MSB contents from 0 to 1 mg/mL. Meanwhile, the emission peaks at  $\sim 422$  and  $\sim 446$  nm gradually became noticeable with the increased *p*-MSB concentrations, which can be ascribed to the stimulated emission from *p*-MSB NPs, as evidenced in Figure S2d [36]. Accordingly, the photoluminescence quantum yield (PLQY) of the as-synthesized 0D–2D heterostructure solution obviously developed as a function of *p*-MSB concentrations, resulting in a 70% increase from 30% to 51%, as shown in Figure 2c. Subsequently, the PLQY of the sample blending with 2 mg/mL *p*-MSB NPs was slightly decreased originating from the saturation of enhanced PL due to the reduced concentration of CsPbBr<sub>3</sub> QDs. With the increased *p*-MSB concentrations, as shown in Figure 2d, the Commission International de L'Eclairage (CIE) chromaticity coordinates slightly developed from (0.156, 0.782) to (0.163, 0.670) within the green region [37], which can further confirm the neglectable effect on color variation with the incorporation of *p*-MSB NPs.

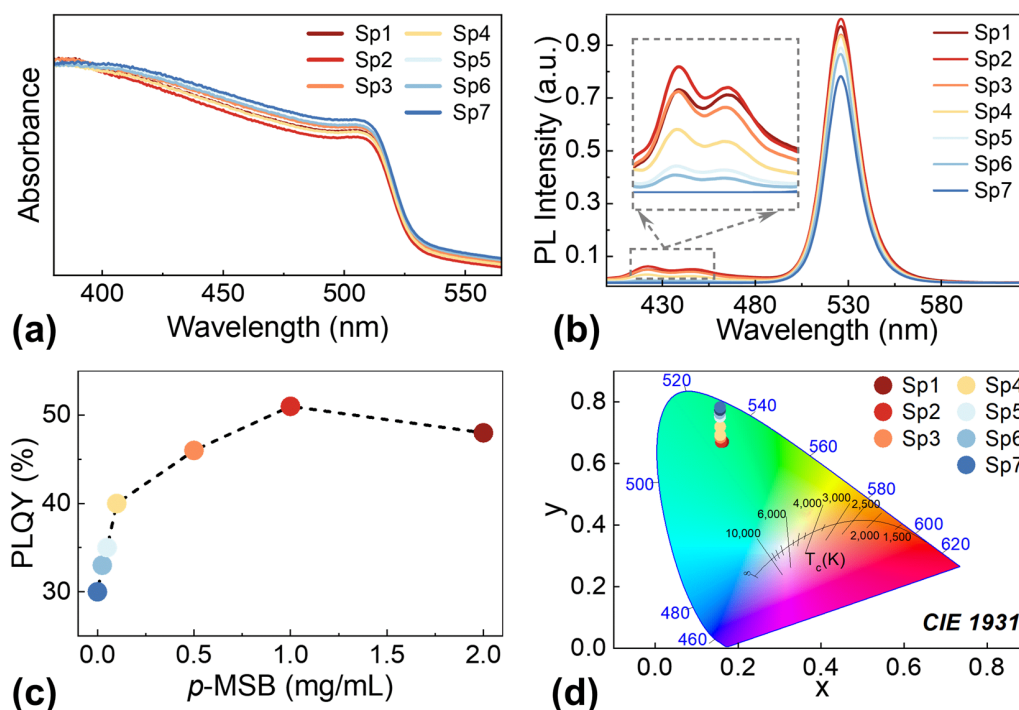


**Figure 2.** (a) Absorption spectra, (b) normalized photoluminescence (PL) spectra, (c) PLQY plots, and (d) CIE coordinates of hybrid CsPbBr<sub>3</sub> QD/*p*-MSB NP solutions with various *p*-MSB concentrations: Sp1 (2 mg/mL), Sp2 (1 mg/mL), Sp3 (0.5 mg/mL), Sp4 (0.1 mg/mL), Sp5 (0.05 mg/mL), Sp6 (0.025 mg/mL), Sp7 (0 mg/mL).

The CsPbBr<sub>3</sub> QD/*p*-MSB NP thin films were fabricated via spin-coating of the 0D–2D heterostructure solutions with a variation of *p*-MSB concentrations. As clearly shown

in Figure 3a–g, the surface morphologies appeared comparable throughout the whole concentration variations, verifying a feasible approach for the fabrication of additional strain-free thin films with enhanced light-emission efficiency. As a result, a comparable root-mean-squared roughness ( $R_{\text{RMS}}$ ) of  $\sim 44$  nm was evenly witnessed with samples as shown in Figure S3. Regardless of the *p*-MSB concentrations, the uniform elementary distribution of Cs, Pb, and Br was observed without any localized aggregations, as revealed in Figures 3h and S4a. Meanwhile, the additional cyan bright spots appeared evenly on the thin films with the increased *p*-MSB concentrations under UV light illumination, as shown in the optical pictures in Figure 3i, which further evidenced the homogenous distribution of *p*-MSB NPs. As shown in Figure S4b,c, the similar atomic ratios were obtained for samples Sp2 (Cs:Pb:Br = 0.59:1:1.85) and Sp7 (Cs:Pb:Br = 0.53:1:1.87), which were in accordance with the stoichiometry of the CsPbBr<sub>3</sub> thin films in previous works [38]. The X-ray-diffraction (XRD) patterns of the samples are presented in Figure 3j, and the peaks appearing at 15.1°, 21.4°, 30.5°, 33.9°, and 37.7° can be assigned to the (100), (110), (200), (210), and (211) planes for the cubic phase of CsPbBr<sub>3</sub>, respectively [39]. The characteristic diffraction peak of the (006) plane for *p*-MSB was observed at 13.6° for the samples with relatively higher *p*-MSB concentrations [40,41]. To further explore the chemistry of *p*-MSB NPs and heterostructure samples, the X-ray photoelectron spectroscopy (XPS) analyses were carried out. The results in Figure S4d,e show that the peak located at 283 eV corresponds to the C 1s of *p*-MSB, while the C 1s peak of Sp7 is located at 284 eV, consistent with previous reports [42]. The position of the C 1s peak in the Sp2 sample is consistent with that in *p*-MSB, suggesting that the composites possess different chemical states with CsPbBr<sub>3</sub> QDs [43]. The Raman spectra of Sp2, Sp7, and *p*-MSB are compared in Figure S4f. The Sp7 shows characteristic peak at 64.7 cm<sup>-1</sup>, which is consistent with previous research [43]. In the case of Sp2, this peak barely shifts, indicating there is no effect of *p*-MSB on the Raman spectra [44]. The evolution of optical properties of the 0D–2D heterostructure thin films as a function of *p*-MSB concentrations is shown in Figure 4. As clearly revealed in Figure 4a, the excitation absorption peak of each sample was similarly observed at 514 nm, which differed from the characteristic peak of *p*-MSB thin films at  $\sim 400$  nm as shown in Figure S5a. An ignorable effect on the crystallinity of CsPbBr<sub>3</sub> thin films by blending with *p*-MSB NPs is suggested, eventually resulting in a comparable optical bandgap of  $\sim 2.36$  eV for each sample, as shown in Figure S5b. Figure S5c describes the contribution of free carriers and excitons to the absorption, which is separated by fitting the experimental data using the Elliott equation [34,45]. By this method, we extracted the exciton resonance ( $E_0$ ) and bandgap energy ( $E_g$ ) that are centered at 2.184 and 2.199 eV, respectively. This renders the exciton binding energy ( $R_{\text{ex}}$ ) to be 15.431 meV. As shown in Figure 4b, the intensity of the emission peak at  $\sim 526$  nm noticeably elevated with the increasing contents of *p*-MSB, and the emission peaks that occurred at  $\sim 461$  and  $\sim 490$  nm can be ascribed to the contribution of the *p*-MSB NPs, as evidenced in Figure S5d. As shown in Figure 4c, the typical type-II heterostructure [46] can be obtained due to the relatively larger bandgap ( $E_g$ ) of *p*-MSB (2.9 eV) [44] than that of CsPbBr<sub>3</sub> (2.3 eV) [47]. Under light illumination, the spontaneous transfer of photogenerated electrons was correspondingly induced by the potential difference between *p*-MSB (conduct band,  $E_C = 2.7$  V) [36] and CsPbBr<sub>3</sub> ( $E_C = 3.6$  V) [48] and the holes collected from CsPbBr<sub>3</sub> to *p*-MSB. Given that the electron mobility of *p*-MSB ( $0.13 \text{ cm}^2 \text{ V}^{-1} \text{ s}^{-1}$ ) [49] was much higher than the hole mobility of CsPbBr<sub>3</sub> ( $0.01 \text{ cm}^2 \text{ V}^{-1} \text{ s}^{-1}$ ) [50], the intensified radiative combination can be expected within CsPbBr<sub>3</sub>, along with the injection of extra electrons. As a result, the PLQY sharply increased from 20% to 40% when the *p*-MSB concentration reached 1 mg/mL, and the saturation of the enhancement in PLQY was witnessed with further increased *p*-MSB concentration due to the dominant charge carrier separation driven by the built-in electric field as shown in Figure 4d. The charge carrier dynamics within the heterostructures were revealed with the time-resolved photoluminescence spectra (TRPL) in Figure 4e, which were fitted with a triexponential decay model by using the Levenberg–Marquardt iteration algorithm.

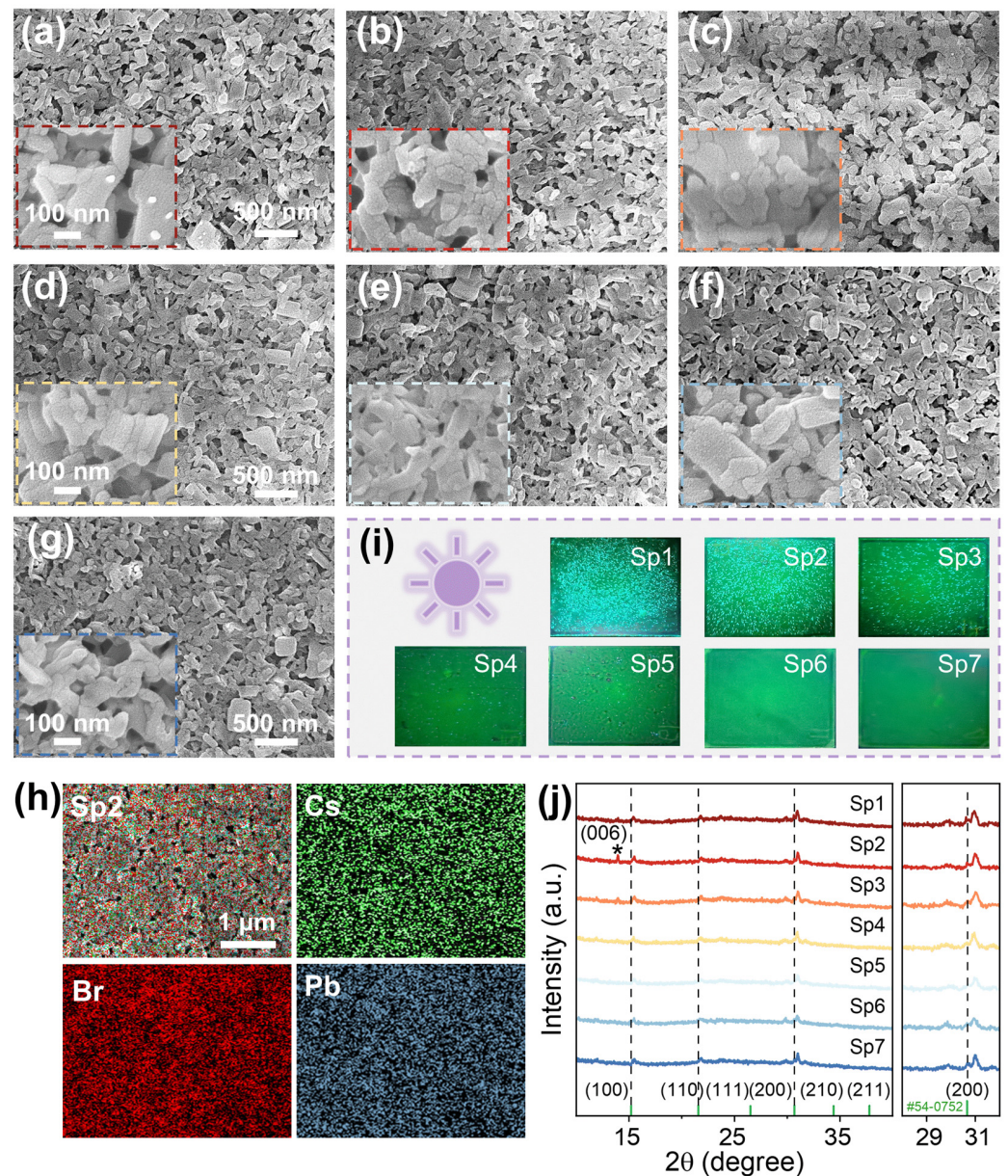


**Figure 3.** Scanning electron microscope (SEM) images of hybrid CsPbBr<sub>3</sub> QD/*p*-MSB NP thin films with different *p*-MSB concentrations: (a) 2 mg/mL (Sp1), (b) 1 mg/mL (Sp2), (c) 0.5 mg/mL (Sp3), (d) 0.1 mg/mL (Sp4), (e) 0.05 mg/mL (Sp5), (f) 0.025 mg/mL (Sp6), (g) 0 mg/mL (Sp7). (h) Energy-dispersive X-ray spectroscopy (EDS) element maps of sample Sp2. (i) The optical pictures of hybrid CsPbBr<sub>3</sub> QD/*p*-MSB NP samples under UV illumination. (j) X-ray diffraction (XRD) spectra of the hybrid CsPbBr<sub>3</sub> QD/*p*-MSB NP thin films (\* marks the position of peak (006)).

$$A = A_1 e^{-t/\tau_1} + A_2 e^{-t/\tau_2} + A_3 e^{-t/\tau_3} \quad (2)$$

Here,  $\tau_1$ ,  $\tau_2$ , and  $\tau_3$  are related to the intrinsic radiative recombination (core state), surface-trap-assisted recombination (shallow level), and non-radiative Shockley–Read–Hall recombination (deep level), respectively [51].  $A_1$ ,  $A_2$ , and  $A_3$  are the corresponding intensities. The fast-decay components (short-lived lifetime)  $\tau_1$  and  $\tau_2$  can be related to the trap-assisted non-radiative recombination at the grain boundaries [52], and thus a shorter period was always witnessed with sample Sp2 ( $\tau_1 = 3.35$  ns,  $\tau_2 = 13.44$  ns) than that of sample Sp7 ( $\tau_1 = 47.61$  ns,  $\tau_2 = 38.28$  ns), suggesting severe defect-related exciton trapping behavior for the pristine CsPbBr<sub>3</sub> QDs, as shown in Table S1. Meanwhile, accelerated radiative recombination was evidenced with a smaller slow-decay component (long-lived

lifetime)  $\tau_3$  of sample Sp7 (5.74 ns) compared with sample Sp2 (6.28 ns) [53]. As revealed in Figure 4f, the chromaticity coordinates of the samples remained in the green region with a slight shift, which was consistent with the evolution witnessed in solutions.

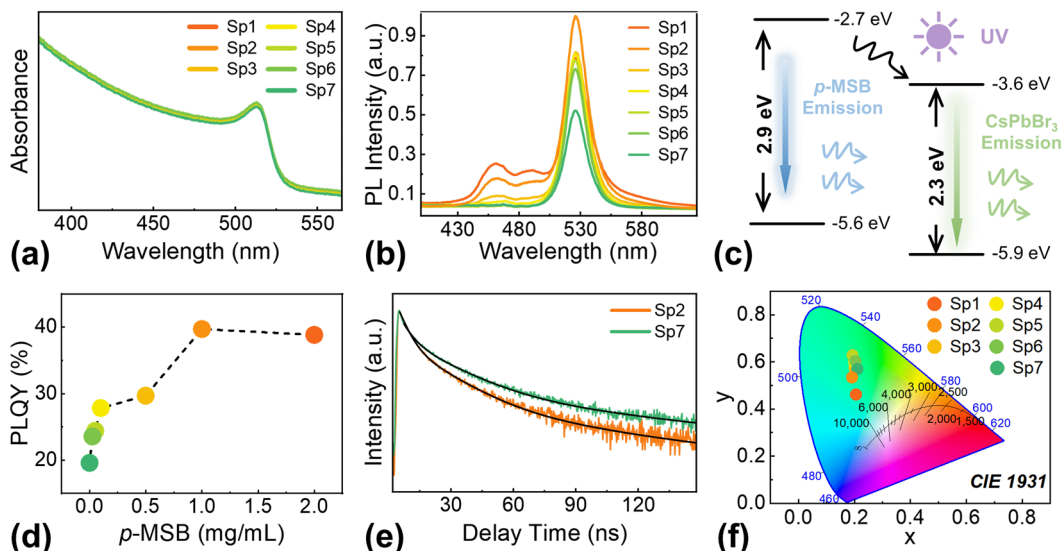


**Figure 4.** (a) Absorption spectra, (b) normalized PL spectra of the hybrid CsPbBr<sub>3</sub> QD/*p*-MSB NP thin films. (c) The energy band diagram under light illumination in the CsPbBr<sub>3</sub> QD/*p*-MSB NP heterostructures. (d) PLQY plots. (e) Time-resolved PL (TRPL) spectra of samples Sp2 and Sp7. (f) CIE coordinates of the hybrid CsPbBr<sub>3</sub> QD/*p*-MSB NP thin films.

The thermal annealing effect on the optical and morphological properties of the 0D–2D heterostructure thin films with an identical *p*-MSB concentration of 1 mg/mL was evaluated by varying the temperatures between 25 and 100 °C. As shown in Figure S6, the grain aggregation of the 0D–2D CsPbBr<sub>3</sub> QD/*p*-MSB NP thin films was gradually observed as a function of temperature, leading to an inclined  $R_{\text{RMS}}$  from 31.0 to 82.5 nm, as revealed in Figure S7. As observed with the XRD patterns in Figure 5a, the characteristic perovskite phase peaks along (100) and (200) slowly became noticeable with the variation in annealing temperatures, and the peak at 12.7° occurred at relatively higher temperatures, manifesting the formation of CsPb<sub>2</sub>Br<sub>5</sub> [54,55]. As shown in Figure S8a, the emission peak at 526 nm was evenly observed with the samples annealed at various temperatures, and the peak intensity gradually increased depending on temperature because of the improved crystallinity [56]. Nevertheless, the damping of PL emission was witnessed with the samples annealed above 60 °C, as shown in Figure S8b, which can be possibly caused by the intensified non-radiative recombination along with the overgrowth of grains [57]. Therefore, the average lifetimes ( $\tau_{\text{avg}}$ ) elongated from 14.15 to 18.97 ns with the elevated temperatures, proving the concurrently boosted recombination for the radiative and non-radiative processes, as shown in Figure 5b and Table S2 [53].

To further estimate the stability for practical applications, the performance of the 0D–2D CsPbBr<sub>3</sub> QD/*p*-MSB NP thin films fabricated with 1 mg/mL *p*-MSB was methodically investigated under diverse conditions, as shown in Figure 5c–g. At room temperature, the sample exhibited excellent stability with a comparable intensity, even after 1 month exposure under an ambient atmosphere as shown in Figure S9, and the slight increase can be possibly attributed to the passivation of adsorbed gas molecules on the surface defects [58]. As shown in Figure S8c,d, continuous post-heating at various temperatures was applied for samples Sp2 and Sp7 to simulate the different temperature working conditions, and the deterioration in PL emission intensity was observed within the whole temperature range between 25 °C and 65 °C. Different from the annealing process during fabrication, the gradual adsorption of gas molecules on the surface defects tended to boost the PL emission owing to the reduced non-radiative recombination centers [59], and the

PL damping can be expected with the exposure of those defects along with the accelerated desorption of the gas molecules [60]. Figure 5c shows that the PL intensity of sample Sp2 decays less with the increase in temperature than that of sample Sp7. Compared with room temperature, the PL intensity remained 58% for sample Sp2 and 34% for sample Sp7 at an identical temperature of 65 °C, indicating the improved thermal stability with the existence of *p*-MSB NPs. It is evident that the *p*-MSB NPs on the surface of the CsPbBr<sub>3</sub> QDs serves as a barrier for oxygen and can block ion migration of inter-particles, thus prohibiting the accompanying ripening growth and PL quenching of the CsPbBr<sub>3</sub> QDs caused by heating [61]. To date, the chronological stability against ambient atmosphere is still a great challenge for perovskite optoelectronic devices due to the undesirable decomposition of perovskite with the corrosion of water molecules [62]. Figures 5d and S10 show the variations in the PL intensity of 0D–2D CsPbBr<sub>3</sub> QD/*p*-MSB NP thin films under low RH (30%), middle RH (75%), and high RH (84%) conditions. The 30%, 75%, and 84% humidity environments are achieved by supersaturated salt solutions of LiF, NaCl, and KCl (25 °C) in a sealed chamber, respectively. As witnessed in Figure 5d, sample Sp2 generally exhibited relatively better stability at each condition owing to the improved stability with *p*-MSB NPs. Thus, the PL intensity of sample Sp2 remains over 74%, and that of sample Sp7 significantly declined by 66% at 75% RH for 12 h due to much more severe decomposition with the formation of by-products based on the Equation (3) [63] as shown in Figure S10a,b.

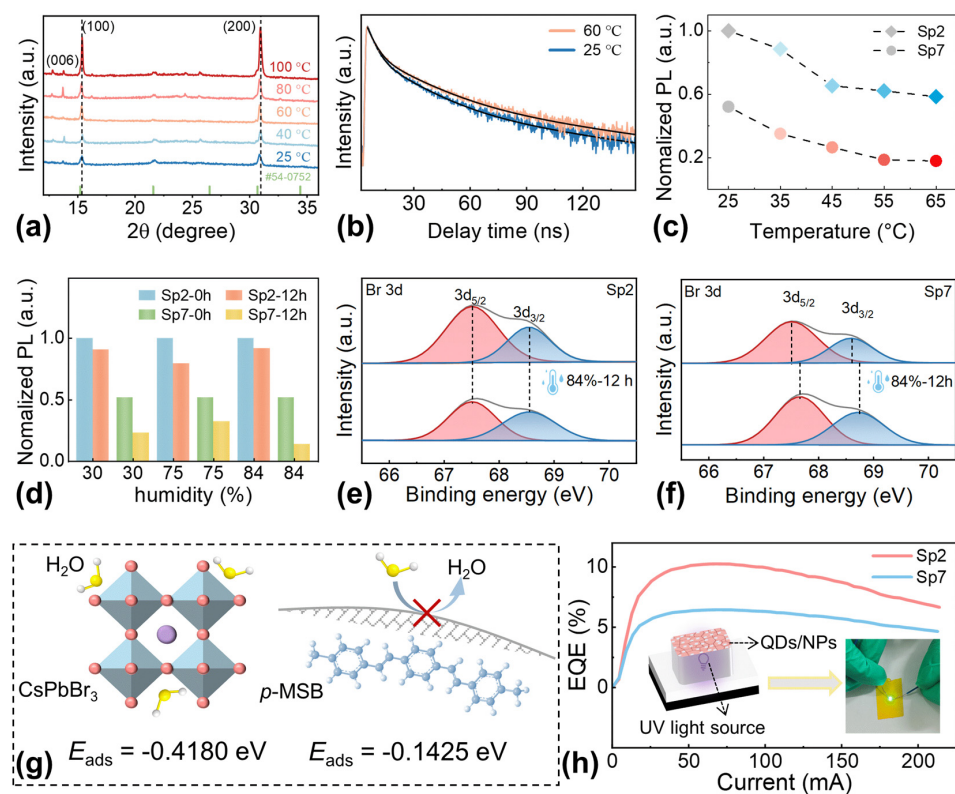
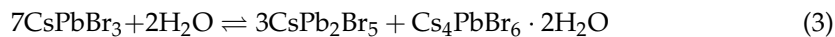
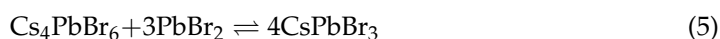
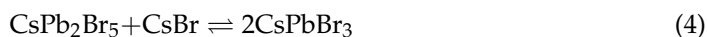


**Figure 5.** (a) XRD spectra and (b) TRPL spectra of the hybrid CsPbBr<sub>3</sub> QD/*p*-MSB NP thin films blending with 1 mg/mL *p*-MSB at different annealing temperatures. (c) The PL intensities as a function of temperatures for samples Sp2 and Sp7. (d) PL intensities of samples Sp2 and Sp7 as fabricated and after storing for 12 h at 30% RH, 75% RH, 84% RH, respectively. (e) X-ray photoelectron spectroscopy (XPS) spectra of Br 3d signatures on sample Sp2 as fabricated and after storing for 12 h at 84% RH. (f) X-ray photoelectron spectroscopy (XPS) spectra of Br 3d signatures on sample Sp7 as fabricated and after storing for 12 h at 84% RH. (g) The calculated adsorption energies ( $E_{\text{ads}}$ ) of H<sub>2</sub>O molecules for the hybrid CsPbBr<sub>3</sub> QD/*p*-MSB NP heterostructures. (h) EQE curve of the Sp2 and Sp7-based LED. (Insets) The configuration and optical image of the LED.



Regardless of the RH, a much more noticeable damping of PL intensity was always observed with sample Sp2 as a function of time in comparison with sample S7 as shown in Figure S10c,d. For sample Sp7, the PL emission peak at 75% RH was continuously higher than 84% RH at each duration, and the opposite trend was observed with sample Sp2, as shown in Figure S10e. It can be because the residual precursors and by-products can be possibly catalyzed into CsPbBr<sub>3</sub> by water molecules under proper humidity based on the following reaction [63]:



Therefore, the crystallinity of CsPbBr<sub>3</sub> was improved by the accelerated ion diffusion of precursors and by-products with the increased RH from 30% to 75%, which can compensate for the damping of PL intensity as shown in Figure 5d [64]. However, the PL intensity of Sp2 at RH 75% was lower than that at RH 30%, which can be caused by the hindrance of ion diffusion with the existence of *p*-MSB. As a result, the PL intensity damping of Sp2 at RH 84% became more moderated than that at RH 75%. With further increased humidity, the decomposition tended to become dominant with the restricted reaction of residual precursors and by-products [65], resulting in a drastic PL intensity damping of Sp2 from 75% RH to 84% RH after 12 h. To verify the moisture effect, Figure 5e,f shows the comparison on the X-ray photoelectron spectroscopy (XPS) spectra of Br 3d signatures for samples Sp2 and Sp7 before and after storing at 84% RH for 12 h, and the Cs 3d and Pb 4f spectra are revealed in Figure S11. As shown in Figure 5e,f, the obvious shifts in the Br 3d<sub>3/2</sub> peak at ~67.5 eV and Br 3d<sub>5/2</sub> peak at ~68.5 eV [66] were concurrently observed with sample Sp7 at 84% RH for 12 h, and the similar behavior was equally witnessed for Pb 4f signatures, as shown in Figure S11, verifying the accelerated generation of derivative-phase CsPb<sub>2</sub>Br<sub>5</sub> and Cs<sub>4</sub>PbBr<sub>6</sub> in Sp7 [67]. Figure S12 shows the full-range survey scan XPS spectra of samples Sp2 and Sp7 as fabricated and after storing for 12 h at 84% RH. Based on the first-principles density functional theory (DFT) calculations, as shown in Figure 5g, the adsorption energies ( $E_{\text{ads}}$ ) of the water molecule on the surfaces of CsPbBr<sub>3</sub> (−0.4180 eV) were much lower than that of *p*-MSB (−0.1425 eV), and thus the hydrophobicity of *p*-MSB can effectively prevent the direct contact of CsPbBr<sub>3</sub> and water molecules, resulting in improved stability for 0D–2D CsPbBr<sub>3</sub> QD/*p*-MSB NP [68]. The TRPL in Figure 4e shows that the heterostructure has fewer non-radiative recombinations caused by defects compared to the original quantum dots. Figures 5e,f and S11 exhibit XPS spectra of Br (67.5 eV, 68.5 eV), Cs (723.8 eV, 737.7 eV) and Pb (137.5 eV, 142.3 eV) elements. Both Sp2 and Sp7 show no obvious peak transformation for Br 3d, Cs 3d, and Pb 4f, indicating no new chemical bonds formed between CsPbBr<sub>3</sub> QDs and *p*-MSB NPs [69]. In other words, *p*-MSB NPs do not passivate CsPbBr<sub>3</sub> QDs by replacing halide defect sites. Thus, *p*-MSB NPs may passivate defects by wrapping on the surface of quantum dots, as shown in Figure 1b, and then prevent the invasion of oxygen and water molecules. Finally, we spin-coated the 0D–2D CsPbBr<sub>3</sub> QD/*p*-MSB NP with the optimized ratio of the UV light source (0603-0.55T, Shenzhen Pink Purple Industrial Co., Ltd., Shenzhen, China) for the fabrication of green LEDs. As shown in Figure 5h, a maximum EQE of 10.26% was obtained, which is higher than the EQE (6.45%) of CsPbBr<sub>3</sub> QDs. As shown in the insets of Figure 5h, the bright-green color was observed by the LED fabricated with the 0D–2D CsPbBr<sub>3</sub> QD/*p*-MSB NPs, indicating the great potential for the application of light sources.

#### 4. Conclusions

In summary, we developed a facile method to prepare highly luminescent and ultra-stable 0D–2D CsPbBr<sub>3</sub> QD/*p*-MSB NP heterostructures under atmospheric conditions. The typical type-II heterostructure spontaneously formed with the in situ nucleation of CsPbBr<sub>3</sub> QDs on *p*-MSB NPs, and the PLQY drastically increased by 200% for a narrow emission band around 526 nm obtained by the heterostructure thin films with 1 mg/mL *p*-MSB than that of the pristine one. Meanwhile, the robust parclose screen constructed with *p*-MSB NPs successfully prevented CsPbBr<sub>3</sub> QDs from attacking with oxygen and moisture, resulting in a comparable PL intensity of the heterostructure thin films under exposure in atmospheric conditions for 1 month. Correspondingly, compared with the pristine sample, relatively less decreases were observed with the heterostructure thin films after continuous post-heating at each temperature, indicating that the existence of *p*-MSB NPs retarded the absorption of gas molecules on the surface defects. Given that the  $E_{\text{ads}}$  of CsPbBr<sub>3</sub> (−0.4180 eV) was much lower than that of *p*-MSB (−0.1425 eV), the PL intensity of the pristine sample severely decreased by 75% after 12 h, and the long-term stability was witnessed with the heterostructure thin films even at RH 84%. Therefore, the synergistic strategy can excellently realize the high PLQY and stability of a perovskite-based light source. To fulfill the practical applications, the green-emitting LED with a high EQE of 9.67% was fabricated based on these QDs/NPs, paving a path for practical applications in UWOC systems.

**Supplementary Materials:** The following supporting information can be downloaded at: <https://www.mdpi.com/article/10.3390/nano13192723/s1>, Figure S1: The selected area electron diffraction (SAED) pattern image of the CsPbBr<sub>3</sub> QD/*p*-MSB NP solutions by blending with 1 mg/mL *p*-MSB; Figure S2: (a) Absorption spectra of *p*-MSB NP solutions. (b) The Tauc plots of CsPbBr<sub>3</sub> QD/*p*-MSB NP solutions. (c) Absorption spectrum and Elliott's model of the CsPbBr<sub>3</sub> QD/*p*-MSB NP solutions by blending with 1 mg/mL *p*-MSB. (d) Normalized PL spectra of *p*-MSB NP solutions; Figure S3: Atomic force microscopy (AFM) images of the samples: (a) Sp2, (b) Sp3, (c) Sp7; Figure S4: (a) Energy-dispersive X-ray spectroscopy (EDS) element maps of sample Sp7. EDS spectra of the samples (b) Sp2 and (c) Sp7. X-ray photoelectron spectroscopy (XPS) spectra of C 1s signatures on the (d) *p*-MSB and (e) samples. (f) Raman spectra of Sp2, Sp7, and *p*-MSB measured with a 532 nm excitation laser; Figure S5: (a) Absorption spectra of *p*-MSB thin films. (b) The Tauc plots of CsPbBr<sub>3</sub> QD/*p*-MSB NP thin films. (c) Absorption spectrum and Elliott's model of the CsPbBr<sub>3</sub> QD/*p*-MSB NP films by blending with 1 mg/mL *p*-MSB. (d) Normalized PL spectra of *p*-MSB thin films; Figure S6: Scanning electron microscope (SEM) images of the hybrid CsPbBr<sub>3</sub> QD/*p*-MSB NP thin films with 1 mg/mL *p*-MSB at different annealing temperatures: (a) 25 °C, (b) 40 °C, (c) 60 °C, (d) 80 °C, and (e) 100 °C; Figure S7: Atomic force microscopy (AFM) of the hybrid CsPbBr<sub>3</sub> QD/*p*-MSB NP thin films with 1 mg/mL *p*-MSB at different annealing temperatures: (a) 25 °C and (b) 60 °C; Figure S8: (a) Normalized room temperature PL spectra and (b) the plots of PL intensities of hybrid CsPbBr<sub>3</sub> QD/*p*-MSB NP thin films with 1 mg/mL *p*-MSB fabricated at different annealing temperatures. Normalized PL spectra of the samples (c) Sp2 and (d) Sp7 after heating at various temperatures; Figure S9: Normalized photoluminescence (PL) spectra of sample Sp2 as fabricated (red) and after storing for 1 month (purple) in atmospheric ambient air; Figure S10: Normalized PL spectra of the sample (a) Sp7 and (b) Sp2 as fabricated and after storing for 12 h at 75% RH. Normalized PL spectra of samples Sp7 and Sp2 at (c) 75% RH and (d) 84% RH. (e) The time-dependent PL intensities as a function of relative humidity of samples Sp2 and Sp7; Figure S11: X-ray photoelectron spectroscopy (XPS) spectra of (a) Cs 3d and (b) Pb 4f signatures on samples Sp2 as fabricated and after storing for 12 h at 84% RH. (f) X-ray photoelectron spectroscopy (XPS) spectra of (c) Cs 3d and (d) Pb 4f signatures on sample Sp7 as fabricated and after storing for 12 h at 84% RH; Figure S12: The full-range survey scan XPS spectra of samples (a) Sp2 and (b) Sp7 as fabricated and after storing for 12 h at 84% RH; Table S1: PL Decay Time Constants ( $\tau_1$ ,  $\tau_2$ , and  $\tau_3$ ) and Average Lifetimes ( $\tau_{\text{avg}}$ ) of Sp2 and Sp7; Table S2: PL Decay Time Constants ( $\tau_1$ ,  $\tau_2$ , and  $\tau_3$ ) and Average Lifetimes ( $\tau_{\text{avg}}$ ) of Sp2 at different annealing temperatures.

**Author Contributions:** M.-y.L. and S.L. (Sisi Liu) participated in the experiment design; M.-y.L., Y.W., S.L. (Shijie Liu) and Y.M. performed the experiment; L.W., B.S. and H.L. participated in data processing and analysis; Y.W., X.W. and X.D. participated in characterization; Y.W. and M.-y.L. wrote the manuscript. All authors have read and agreed to the published version of the manuscript.

**Funding:** This research was funded by the National Key Research and Development Program of China (2021YFF0603500), the National Natural Science Foundation of China (Grant No. 62204180, 11974266, 62075174), Science Foundation of Donghai Laboratory (DH-2022KF01007), the Fundamental Research Funds for the Central Universities (WUT:2021VA056), the National innovation and entrepreneurship training program for college students (S202210497229).

**Data Availability Statement:** The data are available upon reasonable request from the corresponding author.

**Conflicts of Interest:** The authors declare no conflict of interest.

## References

1. Shen, J.; Wang, J.; Yu, C.; Chen, X.; Wu, J.; Zhao, M.; Qu, F.; Xu, Z.; Han, J.; Xu, J. Single LED-based 46-m underwater wireless optical communication enabled by a multi-pixel photon counter with digital output. *Opt. Commun.* **2019**, *438*, 78–82. [[CrossRef](#)]
2. Gussen, C.M.G.; Diniz, P.S.R.; Campos, M.L.R.; Martins, W.A.; Costa, F.M.; Gois, J.N. A Survey of Underwater Wireless Communication Technologies. *J. Commun. Inf. Syst.* **2016**, *31*, 242–255. [[CrossRef](#)]
3. Zeng, Z.; Fu, S.; Zhang, H.; Dong, Y.; Cheng, J. A Survey of Underwater Optical Wireless Communications. *IEEE Commun. Surv. Tutor.* **2017**, *19*, 204–238. [[CrossRef](#)]
4. Saeed, N.; Celik, A.; Al-Naffouri, T.Y.; Alouini, M.-S. Underwater optical wireless communications, networking, and localization: A survey. *Ad Hoc Netw.* **2019**, *94*, 101935. [[CrossRef](#)]
5. Veldhuis, S.A.; Boix, P.P.; Yantara, N.; Li, M.; Sum, T.C.; Mathews, N.; Mhaisalkar, S.G. Perovskite Materials for Light-Emitting Diodes and Lasers. *Adv. Mater.* **2016**, *28*, 6804–6834. [[CrossRef](#)]
6. Ijaz, P.; Imran, M.; Soares, M.M.; Tolentino, H.C.N.; Martin-Garcia, B.; Giannini, C.; Moreels, I.; Manna, L.; Krahe, R. Composition-, Size-, and Surface Functionalization-Dependent Optical Properties of Lead Bromide Perovskite Nanocrystals. *J. Phys. Chem. Lett.* **2020**, *11*, 2079–2085. [[CrossRef](#)]
7. Maddalena, F.; Witkowski, M.E.; Makowski, M.; Bachiri, A.; Mahler, B.; Wong, Y.-C.; Chua, C.Y.E.; Lee, J.X.; Drozdowski, W.; Springham, S.V.; et al. Stable and Bright Commercial CsPbBr<sub>3</sub> Quantum Dot-Resin Layers for Apparent X-ray Imaging Screen. *ACS Appl. Mater. Interfaces* **2021**, *13*, 59450–59459. [[CrossRef](#)]
8. Chen, Q.; Wu, J.; Ou, X.; Huang, B.; Almutlaq, J.; Zhumeckenov, A.A.; Guan, X.; Han, S.; Liang, L.; Yi, Z.; et al. All-inorganic perovskite nanocrystal scintillators. *Nature* **2018**, *561*, 88–93. [[CrossRef](#)]
9. Akhil, S.; Palabathuni, M.; Biswas, S.; Singh, R.; Mishra, N. Highly Stable Amine-Free CsPbBr<sub>3</sub> Perovskite Nanocrystals for Perovskite-Based Display Applications. *ACS Appl. Nano Mater.* **2022**, *5*, 13561–13572. [[CrossRef](#)]
10. Koscher, B.A.; Swabeck, J.K.; Bronstein, N.D.; Alivisatos, A.P. Essentially Trap-Free CsPbBr<sub>3</sub> Colloidal Nanocrystals by Postsynthetic Thiocyanate Surface Treatment. *J. Am. Chem. Soc.* **2017**, *139*, 6566–6569. [[CrossRef](#)]
11. Kim, Y.; Yassitepe, E.; Voznyy, O.; Comin, R.; Walters, G.; Gong, X.; Kanjanaboos, P.; Nogueira, A.F.; Sargent, E.H. Efficient Luminescence from Perovskite Quantum Dot Solids. *ACS Appl. Mater. Interfaces* **2015**, *7*, 25007–25013. [[CrossRef](#)] [[PubMed](#)]
12. Tan, Y.; Zou, Y.; Wu, L.; Huang, Q.; Yang, D.; Chen, M.; Ban, M.; Wu, C.; Wu, T.; Bai, S.; et al. Highly Luminescent and Stable Perovskite Nanocrystals with Octylphosphonic Acid as a Ligand for Efficient Light-Emitting Diodes. *ACS Appl. Mater. Interfaces* **2018**, *10*, 3784–3792. [[CrossRef](#)]
13. Tan, Y.; Li, R.; Xu, H.; Qin, Y.; Song, T.; Sun, B. Ultrastable and Reversible Fluorescent Perovskite Films Used for Flexible Instantaneous Display. *Adv. Funct. Mater.* **2019**, *29*, 1900730. [[CrossRef](#)]
14. Liang, P.; Zhang, P.; Pan, A.; Yan, K.; Zhu, Y.; Yang, M.; He, L. Unusual Stability and Temperature-Dependent Properties of Highly Emissive CsPbBr<sub>3</sub> Perovskite Nanocrystals Obtained from in Situ Crystallization in Poly(vinylidene difluoride). *ACS Appl. Mater. Interfaces* **2019**, *11*, 22786–22793. [[CrossRef](#)] [[PubMed](#)]
15. Zhang, Y.; Zhao, Y.; Wu, D.; Xue, J.; Qiu, Y.; Liao, M.; Pei, Q.; Goorsky, M.S.; He, X. Homogeneous Freestanding Luminescent Perovskite Organogel with Superior Water Stability. *Adv. Mater.* **2019**, *31*, e1902928. [[CrossRef](#)]
16. Leijtens, T.; Eperon, G.E.; Noel, N.K.; Habisreutinger, S.N.; Petrozza, A.; Snaith, H.J. Stability of Metal Halide Perovskite Solar Cells. *Adv. Energy Mater.* **2015**, *5*, 1500963. [[CrossRef](#)]
17. Tang, Y.; Wang, P.; Wang, R.; Yuan, H.; Xin, Y.; Ren, X.; Chen, Q.; Yin, H. Stable MAPbBr<sub>3</sub>@PbBr(OH) composites with high photoluminescence quantum yield: Synthesis, optical properties, formation mechanism, and catalytic application. *Appl. Surf. Sci.* **2023**, *616*, 156442. [[CrossRef](#)]
18. Wei, Y.; Cheng, Z.; Lin, J. An overview on enhancing the stability of lead halide perovskite quantum dots and their applications in phosphor-converted LEDs. *Chem. Soc. Rev.* **2019**, *48*, 310–350. [[CrossRef](#)]

19. Tang, X.; Yang, J.; Li, S.; Liu, Z.; Hu, Z.; Hao, J.; Du, J.; Leng, Y.; Qin, H.; Lin, X.; et al. Single Halide Perovskite/Semiconductor Core/Shell Quantum Dots with Ultrastability and Nonblinking Properties. *Adv. Sci.* **2019**, *6*, 1900412. [[CrossRef](#)]
20. Shao, H.; Bai, X.; Pan, G.; Cui, H.; Zhu, J.; Zhai, Y.; Liu, J.; Dong, B.; Xu, L.; Song, H. Highly efficient and stable blue-emitting CsPbBr<sub>3</sub>@SiO<sub>2</sub> nanospheres through low temperature synthesis for nanoprinting and WLED. *Nanotechnology* **2018**, *29*, 285706. [[CrossRef](#)]
21. Yang, F.; Zhu, J.; Zou, X.; Pang, X.; Yang, R.; Chen, S.; Fang, Y.; Shao, T.; Luo, X.; Zhang, L. Three-dimensional TiO<sub>2</sub>/SiO<sub>2</sub> composite aerogel films via atomic layer deposition with enhanced H<sub>2</sub>S gas sensing performance. *Ceram. Int.* **2018**, *44*, 1078–1085. [[CrossRef](#)]
22. Zhang, Q.; Wang, B.; Zheng, W.; Kong, L.; Wan, Q.; Zhang, C.; Li, Z.; Cao, X.; Liu, M.; Li, L. Ceramic-like stable CsPbBr<sub>3</sub> nanocrystals encapsulated in silica derived from molecular sieve templates. *Nat. Commun.* **2020**, *11*, 31. [[CrossRef](#)] [[PubMed](#)]
23. Wang, S.; Bi, C.; Yuan, J.; Zhang, L.; Tian, J. Original Core–Shell Structure of Cubic CsPbBr<sub>3</sub>@Amorphous CsPbBr<sub>x</sub> Perovskite Quantum Dots with a High Blue Photoluminescence Quantum Yield of over 80%. *ACS Energy Lett.* **2017**, *3*, 245–251. [[CrossRef](#)]
24. Xia, M.; Zhu, S.; Luo, J.; Xu, Y.; Tian, P.; Niu, G.; Tang, J. Ultrastable Perovskite Nanocrystals in All-Inorganic Transparent Matrix for High-Speed Underwater Wireless Optical Communication. *Adv. Opt. Mater.* **2021**, *9*, 2002239. [[CrossRef](#)]
25. Wei, Y.; Deng, X.; Xie, Z.; Cai, X.; Liang, S.; Ma, P.A.; Hou, Z.; Cheng, Z.; Lin, J. Enhancing the Stability of Perovskite Quantum Dots by Encapsulation in Crosslinked Polystyrene Beads via a Swelling-Shrinking Strategy toward Superior Water Resistance. *Adv. Funct. Mater.* **2017**, *27*, 1703535. [[CrossRef](#)]
26. Li, Y.; Fan, Y.; Ma, J. Thermal, physical and chemical stability of porous polystyrene-type beads with different degrees of crosslinking. *Polym. Degrad. Stab.* **2001**, *73*, 163–167. [[CrossRef](#)]
27. Pang, X.; Zhang, H.; Xie, L.; Xuan, T.; Sun, Y.; Si, S.; Jiang, B.; Chen, W.; Zhuang, J.; Hu, C.; et al. Precipitating CsPbBr<sub>3</sub> quantum dots in boro-germanate glass with a dense structure and inert environment toward highly stable and efficient narrow-band green emitters for wide-color-gamut liquid crystal displays. *J. Mater. Chem. C* **2019**, *7*, 13139–13148. [[CrossRef](#)]
28. Zhang, J.; Fan, L.; Li, J.; Liu, X.; Wang, R.; Wang, L.; Tu, G. Growth mechanism of CsPbBr<sub>3</sub> perovskite nanocrystals by a co-precipitation method in a CSTR system. *Nano Res.* **2018**, *12*, 121–127. [[CrossRef](#)]
29. Lou, Y.; Niu, Y.; Yang, D.; Xu, Q.; Hu, Y.; Shen, Y.; Ming, J.; Chen, J.; Zhang, L.; Zhao, Y. Rod-shaped thiocyanate-induced abnormal band gap broadening in SCN<sup>−</sup> doped CsPbBr<sub>3</sub> perovskite nanocrystals. *Nano Res.* **2018**, *11*, 2715–2723. [[CrossRef](#)]
30. Joshi, H.; Thapa, R.K.; Laref, A.; Sukkobot, W.; Pachuau, L.; Vanchhawng, L.; Grima-Gallardo, P.; Musa Saad, H.-E.M.; Rai, D.P. Electronic and optical properties of cubic bulk and ultrathin surface [001] slab of CsPbBr<sub>3</sub>. *Surf. Interfaces* **2022**, *30*, 101829. [[CrossRef](#)]
31. Long, N.; Fu, Y.; Xu, T.; Ding, D.; Zhang, S.; Sun, S.; Kang, S.; Xu, T.; Dai, S.; Nie, Q.; et al. Nanocrystallization and optical properties of CsPbBr<sub>3</sub>–I perovskites in chalcogenide glasses. *J. Eur. Ceram. Soc.* **2021**, *41*, 4584–4589. [[CrossRef](#)]
32. Bera, K.P.; Haider, G.; Huang, Y.T.; Roy, P.K.; Paul Inbaraj, C.R.; Liao, Y.M.; Lin, H.I.; Lu, C.H.; Shen, C.; Shih, W.Y.; et al. Graphene Sandwich Stable Perovskite Quantum-Dot Light-Emissive Ultrasensitive and Ultrafast Broadband Vertical Phototransistors. *ACS Nano* **2019**, *13*, 12540–12552. [[CrossRef](#)] [[PubMed](#)]
33. Hu, G.; Qin, W.; Liu, M.; Ren, X.; Wu, X.; Yang, L.; Yin, S. Scalable room-temperature synthesis of plum-pudding-like Cs<sub>4</sub>PbBr<sub>6</sub>/CsPbBr<sub>3</sub> microcrystals exhibiting excellent photoluminescence. *J. Mater. Chem. C* **2019**, *7*, 4733–4739. [[CrossRef](#)]
34. Yang, Y.; Yang, M.; Zhu, K.; Johnson, J.C.; Berry, J.J.; van de Lagemaat, J.; Beard, M.C. Large polarization-dependent exciton optical Stark effect in lead iodide perovskites. *Nat. Commun.* **2016**, *7*, 12613. [[CrossRef](#)] [[PubMed](#)]
35. Yu, S.; Xu, J.; Shang, X.; Ma, E.; Lin, F.; Zheng, W.; Tu, D.; Li, R.; Chen, X. Unusual Temperature Dependence of Bandgap in 2D Inorganic Lead-Halide Perovskite Nanoplatelets. *Adv. Sci.* **2021**, *8*, 2100084. [[CrossRef](#)]
36. Nakanotani, H.; Kabe, R.; Yahiro, M.; Takenobu, T.; Iwasa, Y.; Adachi, C. Blue-Light-Emitting Ambipolar Field-Effect Transistors Using an Organic Single Crystal of 1,4-Bis(4-methylstyryl)benzene. *Appl. Phys. Express* **2008**, *1*, 091801. [[CrossRef](#)]
37. Song, Y.H.; Park, S.-Y.; Yoo, J.S.; Park, W.K.; Kim, H.S.; Choi, S.H.; Kwon, S.B.; Kang, B.K.; Kim, J.P.; Jung, H.S.; et al. Efficient and stable green-emitting CsPbBr<sub>3</sub> perovskite nanocrystals in a microcapsule for light emitting diodes. *Chem. Eng. J.* **2018**, *352*, 957–963. [[CrossRef](#)]
38. Ruan, L.J.; Tang, B.; Ma, Y. Improving the Stability of CsPbBr<sub>3</sub> Nanocrystals in Ethanol by Capping with PbBr<sub>2</sub>-Adlayers. *J. Phys. Chem. C* **2019**, *123*, 11959–11967. [[CrossRef](#)]
39. Zhihai, W.; Jiao, W.; Yanni, S.; Jun, W.; Yafei, H.; Pan, W.; Nengping, W.; Zhenfu, Z. Air-stable all-inorganic perovskite quantum dot inks for multicolor patterns and white LEDs. *J. Mater. Sci.* **2019**, *54*, 6917–6929. [[CrossRef](#)]
40. Cao, M.; Zhang, C.; Cai, Z.; Xiao, C.; Chen, X.; Yi, K.; Yang, Y.; Lu, Y.; Wei, D. Enhanced photoelectrical response of thermodynamically epitaxial organic crystals at the two-dimensional limit. *Nat. Commun.* **2019**, *10*, 756. [[CrossRef](#)]
41. Baba, K.; Nishida, K. Preparation of 1,4-bis(4-methylstyryl)benzene nanocrystals by a wet process and evaluation of their optical properties. *Nanoscale Res. Lett.* **2014**, *9*, 16. [[CrossRef](#)] [[PubMed](#)]
42. Thapa, S.; Bhardwaj, K.; Basel, S.; Pradhan, S.; Eling, C.J.; Adawi, A.M.; Bouillard, J.-S.G.; Stasiuk, G.J.; Reiss, P.; Pariyar, A.; et al. Long-term ambient air-stable cubic CsPbBr<sub>3</sub> perovskite quantum dots using molecular bromine. *Nanoscale Adv.* **2019**, *1*, 3388–3391. [[CrossRef](#)] [[PubMed](#)]

43. Xin, M.; Fu, Y.; Zhou, Y.; Han, J.; Mao, Y.; Li, M.; Liu, J.; Huang, M. The surface-enhanced Raman scattering of all-inorganic perovskite quantum dots of CsPbBr<sub>3</sub> encapsulated in a ZIF-8 metal–organic framework. *New J. Chem.* **2020**, *44*, 17570–17576. [[CrossRef](#)]
44. Cai, Z.; Cao, M.; Jin, Z.; Yi, K.; Chen, X.; Wei, D. Large photoelectric-gating effect of two-dimensional van-der-Waals organic/tungsten diselenide heterointerface. *NPJ 2D Mater. Appl.* **2018**, *2*, 21. [[CrossRef](#)]
45. Xu, J.; Yu, S.; Shang, X.; Chen, X. Temperature Dependence of Bandgap in Lead-Halide Perovskites with Corner-Sharing Octahedra. *Adv. Photonics Res.* **2022**, *4*, 2200193. [[CrossRef](#)]
46. Wang, Y.; Wang, Q.; Zhan, X.; Wang, F.; Safdar, M.; He, J. Visible light driven type II heterostructures and their enhanced photocatalysis properties: A review. *Nanoscale* **2013**, *5*, 8326–8339. [[CrossRef](#)]
47. Li, X.; Wu, Y.; Zhang, S.; Cai, B.; Gu, Y.; Song, J.; Zeng, H. CsPbX<sub>3</sub> Quantum Dots for Lighting and Displays: Room-Temperature Synthesis, Photoluminescence Superiorities, Underlying Origins and White Light-Emitting Diodes. *Adv. Funct. Mater.* **2016**, *26*, 2435–2445. [[CrossRef](#)]
48. Cen, G.; Liu, Y.; Zhao, C.; Wang, G.; Fu, Y.; Yan, G.; Yuan, Y.; Su, C.; Zhao, Z.; Mai, W. Atomic-Layer Deposition-Assisted Double-Side Interfacial Engineering for High-Performance Flexible and Stable CsPbBr<sub>3</sub> Perovskite Photodetectors toward Visible Light Communication Applications. *Small* **2019**, *15*, e1902135. [[CrossRef](#)]
49. Yasuda, T.; Saito, M.; Nakamura, H.; Tsutsui, T. Organic Field-Effect Transistors Based on Oligo-p-Phenylenevinylene Derivatives. *Jpn. J. Appl. Phys.* **2006**, *45*, L313–L315. [[CrossRef](#)]
50. Dong, Y.; Wang, Y.K.; Yuan, F.; Johnston, A.; Liu, Y.; Ma, D.; Choi, M.J.; Chen, B.; Chekini, M.; Baek, S.W.; et al. Bipolar-shell resurfacing for blue LEDs based on strongly confined perovskite quantum dots. *Nat. Nanotechnol.* **2020**, *15*, 668–674. [[CrossRef](#)]
51. Yang, H.S.; Noh, S.H.; Suh, E.H.; Jung, J.; Oh, J.G.; Lee, K.H.; Jang, J. Enhanced Stabilities and Production Yields of MAPbBr<sub>3</sub> Quantum Dots and Their Applications as Stretchable and Self-Healable Color Filters. *ACS Appl. Mater. Interfaces* **2021**, *13*, 4374–4384. [[CrossRef](#)]
52. Qaid, S.M.H.; Ghaithan, H.M.; Al-Asbahi, B.A.; Aldwayyan, A.S. Ultra-Stable Polycrystalline CsPbBr<sub>3</sub> Perovskite-Polymer Composite Thin Disk for Light-Emitting Applications. *Nanomaterials* **2020**, *10*, 2382. [[CrossRef](#)]
53. Yang, L.; Fu, B.; Li, X.; Chen, H.; Li, L. Poly(vinylidene fluoride)-passivated CsPbBr<sub>3</sub> perovskite quantum dots with near-unity photoluminescence quantum yield and superior stability. *J. Mater. Chem. C* **2021**, *9*, 1983–1991. [[CrossRef](#)]
54. Li, P.; Cheng, Y.; Zhou, L.; Yu, X.; Jiang, J.; He, M.; Liang, X.; Xiang, W. Photoluminescence properties and device application of CsPb<sub>2</sub>Br<sub>5</sub> quantum dots in glasses. *Mater. Res. Bull.* **2018**, *105*, 63–67. [[CrossRef](#)]
55. Wang, L.; Ma, D.; Guo, C.; Jiang, X.; Li, M.; Xu, T.; Zhu, J.; Fan, B.; Liu, W.; Shao, G.; et al. CsPbBr<sub>3</sub> nanocrystals prepared by high energy ball milling in one-step and structural transformation from CsPbBr<sub>3</sub> to CsPb<sub>2</sub>Br<sub>5</sub>. *Appl. Surf. Sci.* **2021**, *543*, 148782. [[CrossRef](#)]
56. Lei, J.; Gao, F.; Wang, H.; Li, J.; Jiang, J.; Wu, X.; Gao, R.; Yang, Z.; Liu, S.F. Efficient planar CsPbBr<sub>3</sub> perovskite solar cells by dual-source vacuum evaporation. *Sol. Energy Mater. Sol. Cells* **2018**, *187*, 1–8. [[CrossRef](#)]
57. Tong, G.; Chen, T.; Li, H.; Qiu, L.; Liu, Z.; Dang, Y.; Song, W.; Ono, L.K.; Jiang, Y.; Qi, Y. Phase transition induced recrystallization and low surface potential barrier leading to 10.91%-efficient CsPbBr<sub>3</sub> perovskite solar cells. *Nano Energy* **2019**, *65*, 104015. [[CrossRef](#)]
58. Yu, M.; He, X.; Li, D.; Lin, J.; Yu, C.; Fang, Y.; Liu, Z.; Guo, Z.; Huang, Y.; Tang, C. Anchoring of CsPbBr<sub>3</sub> perovskite quantum dots on BN nanostructures for enhanced efficiency and stability: A comparative study. *J. Mater. Chem. C* **2021**, *9*, 842–850. [[CrossRef](#)]
59. Song, J.; Li, J.; Xu, L.; Li, J.; Zhang, F.; Han, B.; Shan, Q.; Zeng, H. Room-Temperature Triple-Ligand Surface Engineering Synergistically Boosts Ink Stability, Recombination Dynamics, and Charge Injection toward EQE-11.6% Perovskite QLEDs. *Adv. Mater.* **2018**, *30*, e1800764. [[CrossRef](#)]
60. Liu, J.; Peng, Y.; Zhu, B.; Li, Y.; Zhang, L.; Yu, J. ZIF-8 derived ZnO-CsPbBr<sub>3</sub> polyhedrons for efficient triethylamine detection. *Sens. Actuators B Chem.* **2022**, *357*, 131366. [[CrossRef](#)]
61. Sun, H.; Li, Z.; Kong, L.; Wang, B.; Zhang, C.; Yuan, Q.; Huang, S.; Liu, Y.; Li, L. Enhancing the stability of CsPbBr<sub>3</sub> nanocrystals by sequential surface adsorption of S<sup>2-</sup> and metal ions. *Chem. Commun.* **2018**, *54*, 9345–9348. [[CrossRef](#)]
62. Barbé, J.; Kumar, V.; Newman, M.J.; Lee, H.K.H.; Jain, S.M.; Chen, H.; Charbonneau, C.; Rodenburg, C.; Tsoi, W.C. Dark electrical bias effects on moisture-induced degradation in inverted lead halide perovskite solar cells measured by using advanced chemical probes. *Sustain. Energy Fuels* **2018**, *2*, 905–914. [[CrossRef](#)]
63. Di Girolamo, D.; Dar, M.I.; Dini, D.; Gontrani, L.; Caminiti, R.; Mattoni, A.; Graetzel, M.; Meloni, S. Dual effect of humidity on cesium lead bromide: Enhancement and degradation of perovskite films. *J. Mater. Chem. A* **2019**, *7*, 12292–12302. [[CrossRef](#)]
64. Duan, J.; Zhao, Y.; He, B.; Tang, Q. High-Purity Inorganic Perovskite Films for Solar Cells with 9.72% Efficiency. *Angew. Chem. Int. Ed.* **2018**, *57*, 3787–3791. [[CrossRef](#)]
65. Sandeep, K. CsPbBr<sub>3</sub> perovskite nanocrystals coated paper substrate as atmospheric humidity sensor. *Mater. Today Proc.* **2021**, *41*, 610–612. [[CrossRef](#)]
66. Xu, F.; Meng, K.; Cheng, B.; Wang, S.; Xu, J.; Yu, J. Unique S-scheme heterojunctions in self-assembled TiO<sub>2</sub>/CsPbBr<sub>3</sub> hybrids for CO<sub>2</sub> photoreduction. *Nat. Commun.* **2020**, *11*, 4613. [[CrossRef](#)]
67. Li, H.; Tong, G.; Chen, T.; Zhu, H.; Li, G.; Chang, Y.; Wang, L.; Jiang, Y. Interface engineering using a perovskite derivative phase for efficient and stable CsPbBr<sub>3</sub> solar cells. *J. Mater. Chem. A* **2018**, *6*, 14255–14261. [[CrossRef](#)]

68. Shan, Q.; Li, J.; Song, J.; Zou, Y.; Xu, L.; Xue, J.; Dong, Y.; Huo, C.; Chen, J.; Han, B.; et al. All-inorganic quantum-dot light-emitting diodes based on perovskite emitters with low turn-on voltage and high humidity stability. *J. Mater. Chem. C* **2017**, *5*, 4565–4570. [[CrossRef](#)]
69. Yang, H.; Yin, W.; Dong, W.; Gao, L.; Tan, C.-H.; Li, W.; Zhang, X.; Zhang, J. Enhancing the light-emitting performance and stability in CsPbBr<sub>3</sub> perovskite quantum dots via simultaneous doping and surface passivation. *J. Mater. Chem. C* **2020**, *8*, 14439–14445. [[CrossRef](#)]

**Disclaimer/Publisher's Note:** The statements, opinions and data contained in all publications are solely those of the individual author(s) and contributor(s) and not of MDPI and/or the editor(s). MDPI and/or the editor(s) disclaim responsibility for any injury to people or property resulting from any ideas, methods, instructions or products referred to in the content.